

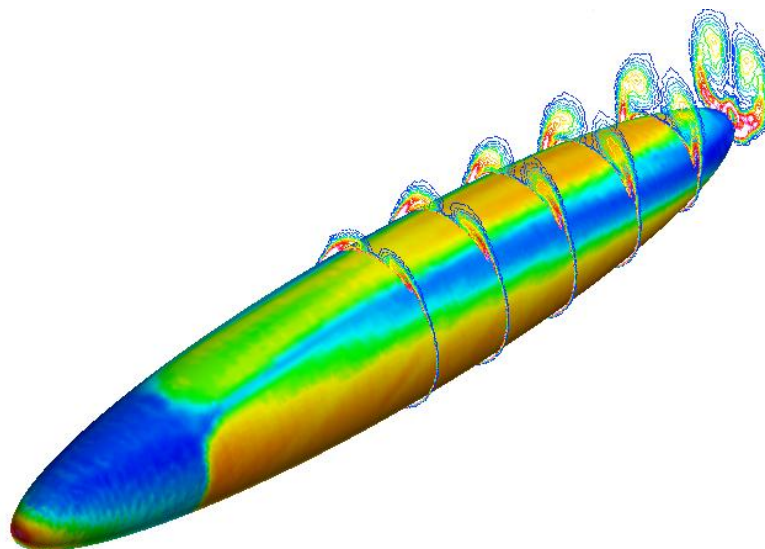


**AIAA 2003-0269**

**Prediction of a Prolate Spheroid  
Undergoing a Pitchup Maneuver**

Rupesh B. Kotapati-Apparao, Kyle D. Squires  
*MAE Department, Arizona State University, Tempe, AZ*

James R. Forsythe  
*United States Air Force Academy, Colorado Springs, CO*



**Aerospace Sciences Meeting 2003  
6-9 January 2003 / Reno, Nevada**

# Prediction of a Prolate Spheroid Undergoing a Pitchup Maneuver

Rupesh B. Kotapati-Apparao\*, Kyle D. Squires†  
*MAE Department, Arizona State University, Tempe, AZ*

James R. Forsythe‡  
*United States Air Force Academy, Colorado Springs, CO*

Prediction of the time-dependent flow around a 6 : 1 prolate spheroid undergoing a pitchup maneuver were obtained using Detached-Eddy Simulation (DES). The spheroid pitches about its centroid from 0° to 30° angle of attack at a dimensionless rate of 0.047 (based on the freestream speed and model length). Flowfield predictions are evaluated using experimental measurements and also contrasted against predictions of the flows at static angles of attack ( $\alpha$ ) of 10, 20, and 30°. Flowfield parameters are the same as in the experiments, the Reynolds number based on freestream velocity and the model length is  $4.2 \times 10^6$ , the boundary layers on the spheroid surface are tripped at  $x/L = 0.2$ . Solutions of the compressible Navier-Stokes equations are obtained on unstructured grids, rigid-body motion of the spheroid is accomplished using an Arbitrary Lagrangian Eulerian formulation. Compared to solutions at fixed angle of attack, the flow structure for the pitchup case lags that of the static- $\alpha$  flows. Surface flows for the static- and maneuvering-geometry solutions show marked differences at the conclusion of the pitchup. At 20° angle of attack the pitchup solution does not possess a secondary separation as in the static- $\alpha$  case. Skin friction predictions exhibit similar variation as the experimental measurements of Wetzal and Simpson [1], though are shifted below the measured values. Predictions of the azimuthal pressure distribution exhibits good agreement with the measurements of Hoang *et al.* [2]. Development of the normal force and pitching moment for the maneuvering geometry also show reasonable agreement with measured values.

## Introduction

**E**XTENDING the dynamic performance of aero- and hydro-dynamic vehicles beyond conventional regimes constitutes an area of significant scientific interest and technological importance. Accurate predictive methodologies offer a powerful tool for analysis and improving design, though the flows around bodies experiencing motion are complex and challenge all aspects of numerical simulation approaches. Most of the flows of practical interest occurring at high Reynolds number, are often unsteady, and may experience regions of flow separation. This contribution is relevant to the subset of vehicles experiencing a prescribed motion and for which the objective is prediction of the resulting external flow. In other instances, variations in the external flow can induce motion of a vehicle, a related area of interest (e.g., see Forsythe *et al.* [3]).

The present work focuses on the flow around a prolate spheroid at angle of attack. Unlike in axisymmetric flows in which flow features are often similar to those in two-dimensional configurations, the flow over a spheroid at incidence poses additional complexities.

Along the axial direction, a favorable pressure gradient exists on the windward side, with an adverse pressure gradient along the leeward side of the spheroid. In the circumferential direction, the pressure gradient from the windward to leeward side is favorable over the front half of the body, becoming adverse over the rear half. Several measurements and simulations of the flow over prolate spheroids have documented surface properties, e.g., pressure and skin friction, mean flow and turbulence profiles, and development of the vortical structures that characterizes the separated region at various angles of attack (Ref. [4], [5], [6], [7], [8] and references therein).

For the static-geometry spheroid, an array of simulation techniques have been employed ranging from steady Reynolds-averaged Navier-Stokes (RANS), unsteady RANS (URANS), Large Eddy Simulation (LES), and Detached Eddy Simulation (DES) [9], [10], [11], [12]. In general, previous numerical investigations of static-geometry spheroids have yielded many of the same effects observed in experiments, e.g., fairly accurate predictions of the location of primary and secondary separation for the spheroid at 20° angle of attack [12].

The flowfield around maneuvering bodies has been less researched, both experimentally and numerically. Based on experimental measurements of a 6:1 prolate spheroid undergoing a pitchup-maneuver, Hoang *et al.*

---

\*Graduate Research Assistant

†Professor, AIAA Member, author to whom correspondence should be addressed

‡AIAA Senior Member, present affiliation: Cobalt Solutions LLC

Copyright © 2003 by the American Institute of Aeronautics and Astronautics, Inc. All rights reserved.

*al.* [2] concluded that the flow was highly unsteady and would be difficult to model as steady or even quasi-steady. Wetzel and Simpson [1] also measured the flowfield around a spheroid undergoing transient maneuvers, showing that at higher angles of attack, development of the flow structure lags that characterizing the flow around static geometries at the same angle of attack. The location of primary separation, for example, was delayed at most positions along the spheroid by as much as  $10^\circ$  compared with the measurements of the flow at static angles of attack.

Rhee and Hino [13] recently reported computations of the time-dependent flow around a spheroid undergoing a pitchup maneuver, modeling the configuration measured by Hoang *et al.* [2] and Wetzel and Simpson [1]. In their work, flowfield predictions were obtained via solution of the unsteady RANS equations. A body force term was added to the Navier-Stokes equations to take into account the inertial motion of the coordinate system. Comparisons with experimental data showed similar features to those observed in experiments, e.g., primary separation further leeward compared to the static- $\alpha$  configurations. Rhee and Hino [13] attributed discrepancy between simulation and measurements to modeling errors, pointing out that application of scalar eddy viscosity was not sufficient for adequate resolution of the vortical flow on the leeward side of the body.

For high Reynolds number prediction, RANS methods have traditionally been employed, one advantage being the computational efficiency of such approaches. For attached boundary layers and other thin shear layers not far from their calibration range, RANS models are often adequate. In separated flows, the performance RANS models is often uneven. LES offers a powerful approach for direct resolution of the unsteady features characterizing separated regions. The computational cost of the method, however, prohibits its application to high Reynolds number flows [14]. These considerations provide the primary rationale for the application and continued development of hybrid techniques that combine RANS and LES.

The aim of the present contribution is prediction of the flow around the prolate spheroid undergoing a pitchup about its centroid. The computational approach is based on a RANS-LES hybrid: Detached-Eddy Simulation (DES). DES was originally proposed for application to massively separated flows and to date has yielded predictions of an array of complex flows with comparable or superior accuracy to URANS and at Reynolds numbers for which LES is not feasible. Three-dimensional separated flows as occur over a spheroid at incidence provide a challenging test case since the wake region is not established via the breakdown of overwhelming new instabilities that result in rapid development of chaotic structures in the wake. Three-dimensional separations and similar flows (or re-

gions of a flow) constitute a “grey area” for hybrid methods such as DES in which turbulent eddies may not rapidly develop following boundary layer detachment. The Reynolds-averaged treatment suppresses substantial eddy content near solid surfaces and the lack of structural features in the detaching boundary layers may contribute to more substantial errors in spheroid predictions as compared to other separated flows, especially those experiencing massive separation. The present effort assists in evaluating the current state of approaches for predicting the flow around a maneuvering body and, in addition, aspects of the numerical approach used to compute rigid-body motion. As described in greater detail below, the parameter settings are the same as considered by Hoang *et al.* [2], Wetzel and Simpson [1], and Rhee and Hino [13], enabling an assessment of simulation results against these previous works.

## Approach

### Detached-Eddy Simulation

Flowfield predictions are obtained for both static and maneuvering configurations using Detached-Eddy Simulation (DES). The DES formulation is based on a modification to the Spalart-Allmaras [15] model (referred to as S-A throughout) such that it reduces to its RANS formulation close to solid surfaces and becomes a Large-Eddy Simulation in other regions provided the grid density is sufficient [16]. The S-A RANS model [15] is summarized below along with issues related to the DES formulation. Additional discussion can be found in Spalart [14] and Strelets [17].

In the S-A RANS model, a transport equation is used to compute a working variable used to form the turbulent eddy viscosity,

$$\begin{aligned} \frac{D\tilde{\nu}}{Dt} &= c_{b1}[1 - f_{t2}]\tilde{S}\tilde{\nu} - \left[ c_{w1}f_w - \frac{c_{b1}}{\kappa^2}f_{t2} \right] \left[ \frac{\tilde{\nu}}{d} \right]^2 \\ &+ \frac{1}{\sigma} \left[ \nabla \cdot ((\nu + \tilde{\nu})\nabla\tilde{\nu}) + c_{b2}(\nabla\tilde{\nu})^2 \right] \\ &+ f_{t1} \Delta U^2, \end{aligned} \quad (1)$$

where  $\tilde{\nu}$  is the working variable. The eddy viscosity  $\nu_t$  is obtained from,

$$\nu_t = \tilde{\nu} f_{v1}, \quad f_{v1} = \frac{\chi^3}{\chi^3 + c_{v1}^3}, \quad \chi \equiv \frac{\tilde{\nu}}{\nu}, \quad (2)$$

where  $\nu$  is the molecular viscosity. The production term is expressed as,

$$\tilde{S} \equiv f_{v3}S + \frac{\tilde{\nu}}{\kappa^2 d^2} f_{v2}, \quad f_{v2} = \left( 1 + \frac{\chi}{c_{v2}} \right)^{-3}, \quad (3)$$

where  $S$  is the magnitude of the vorticity. The function  $f_w$  is given by,

$$f_w = g \left[ \frac{1 + c_{w3}^6}{g^6 + c_{w3}^6} \right]^{1/6}, \quad (4)$$

$$g = r + c_{w2} (r^6 - r), \quad r \equiv \frac{\tilde{\nu}}{\tilde{S}\kappa^2 d^2}. \quad (5)$$

The function  $f_{t2}$  is defined as,

$$f_{t2} = c_{t3} \exp(-c_{t4} \chi^2). \quad (6)$$

The trip function  $f_{t1}$  is specified in terms of the distance  $d_t$  from the field point to the trip, the wall vorticity  $\omega_t$  at the trip, and  $\Delta U$  which is the difference between the velocity at the field point and that at the trip,

$$f_{t1} = c_{t1} g_t \exp\left(-c_{t2} \frac{\omega_t^2}{\Delta U^2} [d^2 + g_t^2 d_t^2]\right), \quad (7)$$

where  $g_t = \min(0.1, \Delta U / \omega_t \Delta x)$  and  $\Delta x$  is the grid spacing along the wall at the trip. The solid wall boundary condition is  $\tilde{\nu} = 0$  and the constants are  $c_{b1} = 0.1355$ ,  $\sigma = 2/3$ ,  $c_{b2} = 0.622$ ,  $\kappa = 0.41$ ,  $c_{w1} = c_{b1}/\kappa^2 + (1 + c_{b2})/\sigma$ ,  $c_{w2} = 0.3$ ,  $c_{w3} = 2$ ,  $c_{v1} = 7.1$ ,  $c_{v2} = 5$ ,  $c_{t1} = 1$ ,  $c_{t2} = 2$ ,  $c_{t3} = 1.1$ , and  $c_{t4} = 2$ .

The DES formulation is obtained by replacing in the S-A model the distance to the nearest wall,  $d$ , by  $\tilde{d}$ , where  $\tilde{d}$  is defined as,

$$\tilde{d} \equiv \min(d, C_{DES} \Delta), \quad (8)$$

where  $\Delta$  is the largest distance between the cell center under consideration and the cell center of the neighbors (i.e., those cells sharing a face with the cell in question). In ‘‘natural’’ applications of DES, the wall-parallel grid spacings (e.g., streamwise and spanwise) are on the order of the boundary layer thickness and the S-A RANS model is retained throughout the boundary layer, i.e.,  $\tilde{d} = d$ . Empirical input is strong in the sense that prediction of boundary layer separation is under control of the RANS model in natural DES applications. Away from solid boundaries, the closure is a one-equation model for the SGS eddy viscosity. When the production and destruction terms of the model are balanced, the length scale  $\tilde{d} = C_{DES} \Delta$  in the LES region yields a Smagorinsky-like eddy viscosity  $\tilde{\nu} \propto S \Delta^2$ . Analogous to classical LES, linking the eddy viscosity to  $\Delta$  allows an energy cascade down to the grid size. The additional model constant  $C_{DES} = 0.65$  was set in homogeneous turbulence [18] and used without modification in this work.

### Simulation overview

The compressible Navier-Stokes equations are solved on unstructured grids using Cobalt [19], a commercial version of Cobalt<sub>60</sub>, the Navier-Stokes solver developed at the Air Force Research Laboratory. The numerical method is a cell-centered finite volume approach applicable to arbitrary cell topologies (e.g., hexahedrals, prisms, tetrahedrons). The spatial operator uses the exact Riemann Solver of Gottlieb

and Groth [20], least squares gradient calculations using QR factorization to provide second order accuracy in space, and TVD flux limiters to limit extremes at cell faces. A point implicit method using analytic first-order inviscid and viscous Jacobians is used for advancement of the discretized system. For time-accurate computations, a Newton sub-iteration scheme is employed, the method is second order accurate in time. The domain decomposition library ParMETIS [21] is used for parallel implementation and provides optimal load balancing with a minimal surface interface between zones. Communication between processors is achieved using Message Passing Interface.

A key feature in the commercial version of Cobalt is the capability of computing the flow around geometries undergoing rigid body motion. Simulation of rigid body motion is achieved through an Arbitrary Lagrangian Eulerian (ALE) formulation, where the grid is neither stationary nor follows the fluid motion. The conservation equations are solved in an inertial reference frame with modifications to the spatial operator in order that the advection terms are relative to the (non-inertial) grid reference frame. This requires simple modifications to many boundary conditions and to the initial conditions for the Riemann problem. The ALE formulation also requires modifications to the time-centered implicit temporal operator. A number of Newton sub-iterations are used to reduce errors associated with integrating over the time-step with an implicit temporal operator.

The maneuver is a pitchup of the spheroid about its centroid from  $0^\circ$  to  $30^\circ$  angle of attack at a rate of  $90^\circ$  per second, corresponding to a dimensionless pitch rate of 0.047 based on the spheroid length and freestream speed [1]. The Reynolds number based on freestream velocity and the model length is  $4.2 \times 10^6$ , well above the established critical Reynolds number of  $2.5 \times 10^6$  [5]. As in the experiments, the boundary layer is tripped at  $x/L = 0.2$ .

Unstructured grids were created using VGRIDns developed at the NASA-Langley Research Center [22]. The mesh for the predictions presented in this manuscript was comprised of slightly over  $5.2 \times 10^6$  cells, the grid comprised of prisms in the boundary layer and tetrahedra in other regions (see Figure 1). The distance from the spheroid surface to first cell center was within one viscous unit, geometric stretching at a rate 1.2 was used away from the wall. The timestep, made dimensionless using the minor axis of the spheroid and freestream velocity, was equal to 0.01. In the calculations, the inflow eddy viscosity was set to zero, with the trip terms active on the surface of the spheroid at  $x/L = 0.2$ . Far-field boundary values are obtained from modified Riemann invariants, no-slip conditions are imposed on the spheroid surface.

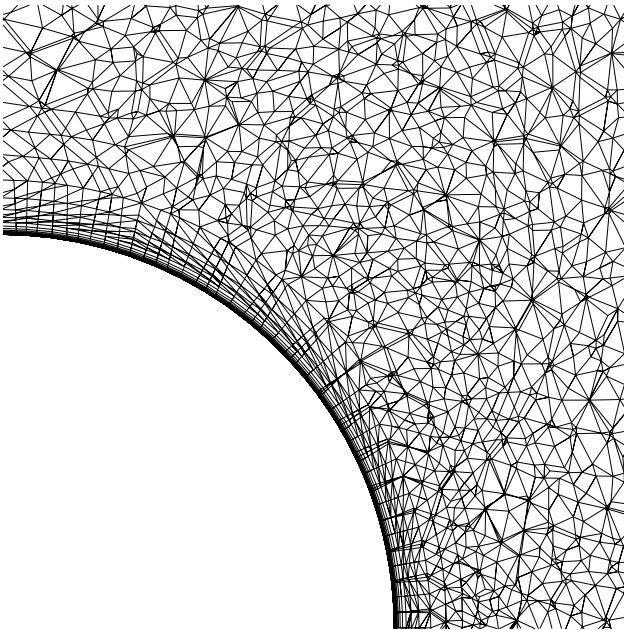
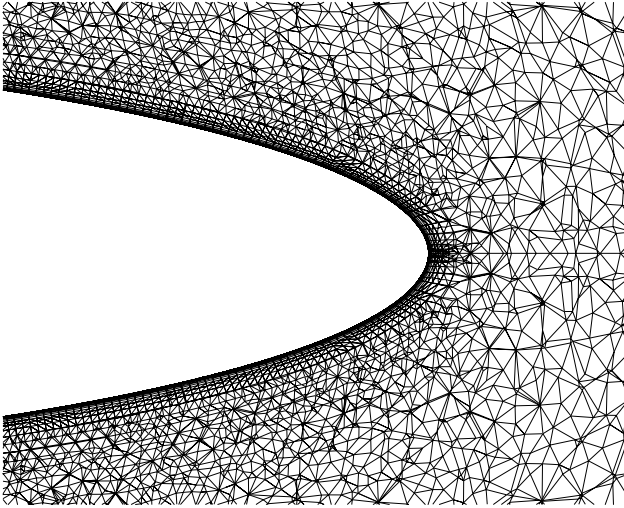


Fig. 1 6:1 prolate spheroid, side and end views of the unstructured grid.

## Results

### Flow visualizations

Figure 2 and Figure 3 show surface flows for the static and pitching geometries at  $20^\circ$  and  $30^\circ$  angle of attack, respectively. For the spheroid at incidence, surface streamlines diverge from the windward plane of symmetry around the spheroid, separation is marked by the convergence of the surface flows, reattachment is identified by the divergence of the surface flows. In the lee side, streamlines from the windward and leeward sides converge to form the primary separation line. For the static geometry at  $\alpha = 20^\circ$ , the primary separation is initiated at an axial location around  $x/L = 0.4$ . At  $30^\circ$  angle of attack, the primary separation is essentially initiated shortly after the boundary layer trip at  $x/L = 0.2$ . Increase in  $\alpha$  leads to more substantial divergence of the flow from the windward

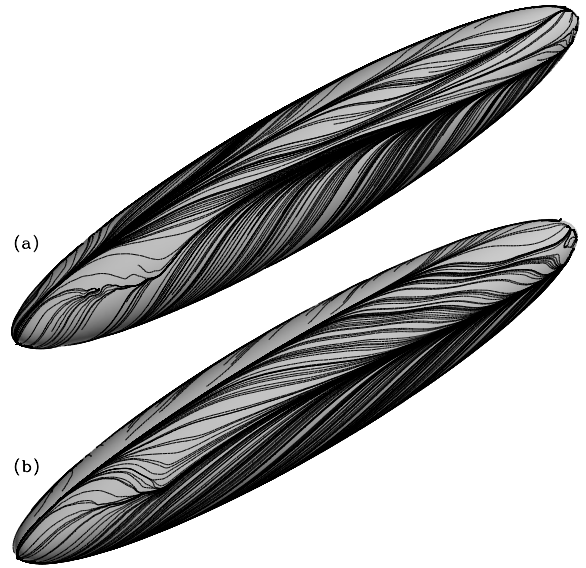


Fig. 2 Surface flows at  $20^\circ$  angle of attack. (a) static, (b) pitchup.

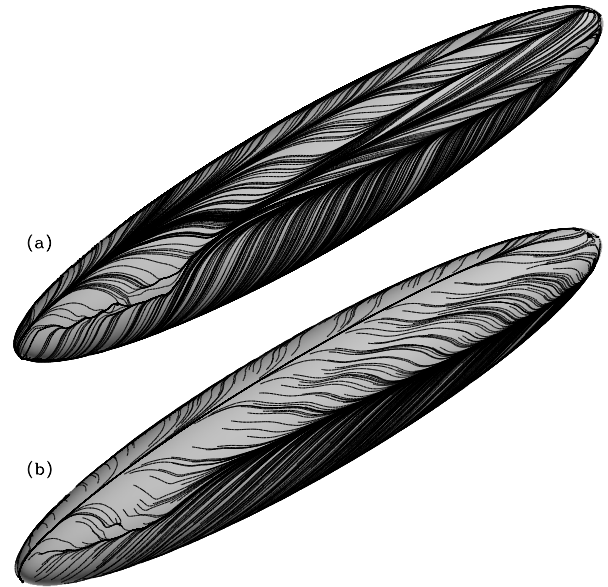
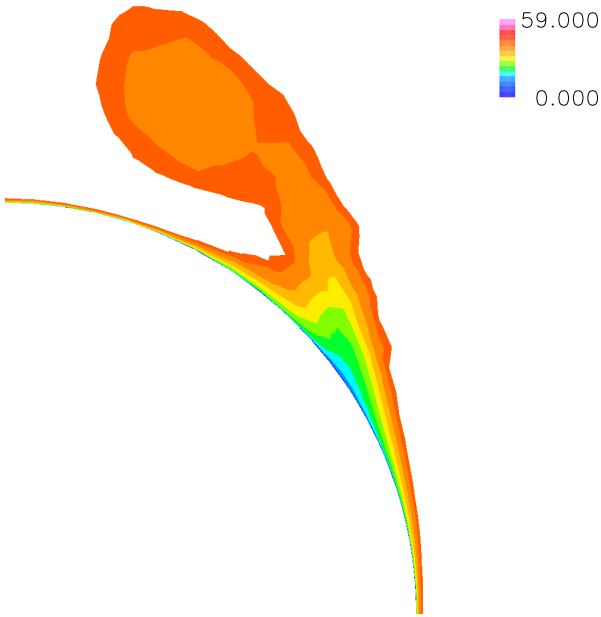


Fig. 3 Surface flows at  $30^\circ$  angle of attack. (a) static, (b) pitchup.

plane of symmetry and for the static- $\alpha$  cases at both  $20^\circ$  and  $30^\circ$ , a reasonably well-developed secondary separation and reattachment is apparent in Figure 2a and Figure 3a. Figure 2b, showing the surface flows for the pitchup at  $\alpha = 20^\circ$ , do indicate the presence of a secondary separation.

In general, the surface flows in Figure 2b and Figure 3b show that angle of attack is effectively lowered by the pitchup compared to the static geometries. As discussed by Wetzel and Simpson [1], for the pitchup case fluid particles experience a less severe adverse



**Fig. 4** Contours of the velocity magnitude in the flow undergoing the pitchup maneuver,  $x/L = 0.772$ ,  $\alpha = 20^\circ$ . Flow separation occurs at approximately  $\phi = 115^\circ$ .

pressure gradient with the boundary layer separation occurring further leeward compared to the static- $\alpha$  cases. For the present calculation, the azimuthal location of the primary separation is further leeward by approximately five degrees, less than the azimuthal change noted by Wetzels and Simpson [1] that was closer to  $10^\circ$ .

An aspect of the structure of the separated region noted in static- $\alpha$  configurations is a low-velocity trough of fluid immediately leeward of separation for all angles of attack [11] [23]. This effect is shown in figure 4 for the pitchup case at  $\alpha = 20^\circ$  and  $x/L = 0.772$ . As discussed by Hedin *et al.* [11], this low-velocity trough is caused by a sweeping up of the low-momentum fluid near the wall by the primary vortices and subsequent accumulation of this fluid between the primary vortex and the body surface. The vorticity contours in Figure 5 show the development of the structures from the primary separation along the lee side for the static- $\alpha$  and pitchup cases at  $20^\circ$  angle of attack. The skin friction contours on the spheroid surface show the influence of the boundary layer trip at  $x/L = 0.2$ . The primary vortex is relatively flat/elliptic and located close to the hull in the first cross-section. With downstream development, the vortex grows in size becoming more circular and in the aft cross-sections the vortex detaches completely from the body surface. A thick longitudinal band of  $C_f$  minima extends from  $x/L = 0.2$  to the rear of the spheroid. The windward edge of this band corresponds to the primary separation lines in both the static and pitching geometries while the leeward edge to the sec-

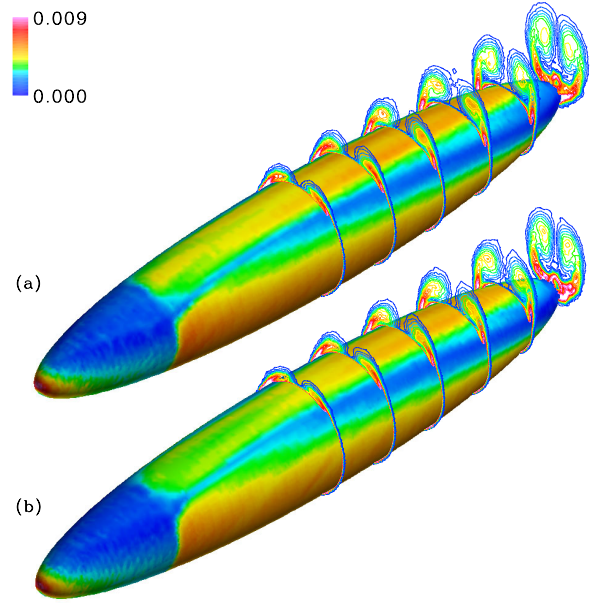


**Fig. 5** Contours of vorticity magnitude at six axial stations, skin friction shown on spheroid surface,  $20^\circ$  angle of attack. (a) static, (b) pitchup.

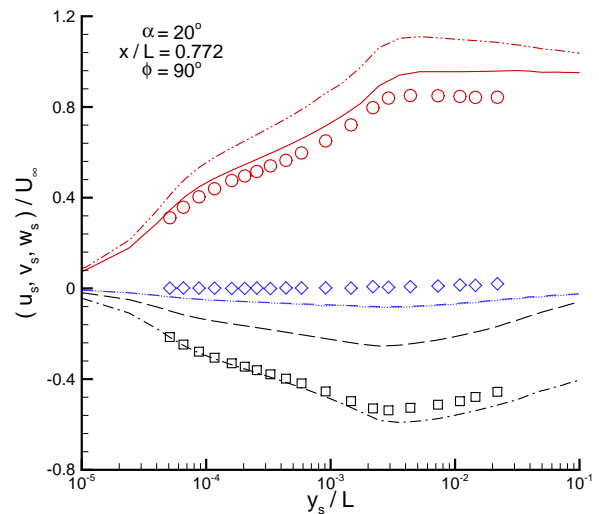


**Fig. 6** Mean velocity profiles for the static and maneuvering geometries at  $20^\circ$  angle of attack, streamwise location  $x/L = 0.772$ , azimuthal angle of  $\phi = 90^\circ$ . Static geometry, DES: —  $u_s/U_\infty$ ; - - -  $v_s/U_\infty$ ; - · -  $w_s/U_\infty$ . Maneuvering geometry, DES: - · -  $u_s/U_\infty$ ; · · ·  $v_s/U_\infty$ ; - - -  $w_s/U_\infty$ . Static geometry, measurements:  $\circ$   $u_s/U_\infty$ ;  $\diamond$   $v_s/U_\infty$ ;  $\square$   $w_s/U_\infty$ .

ondary separation line in the static flow

### Mean velocity profiles

Velocity profiles are shown in a reference frame attached to the spheroid and aligned with the local coordinates (body axis). The  $u_s$  component is tangent to the spheroid surface and aligned with the major axis.

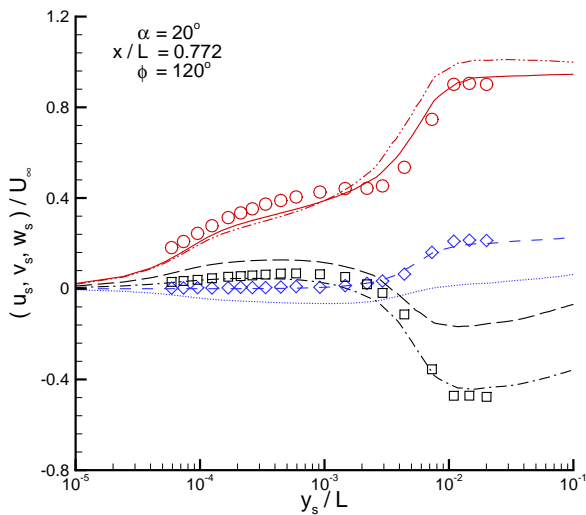


**Fig. 7** Mean velocity profiles for the static and maneuvering geometries at  $20^\circ$  angle of attack, streamwise location  $x/L = 0.772$ , azimuthal angle of  $\phi = 120^\circ$ . Legend same as Figure 6.

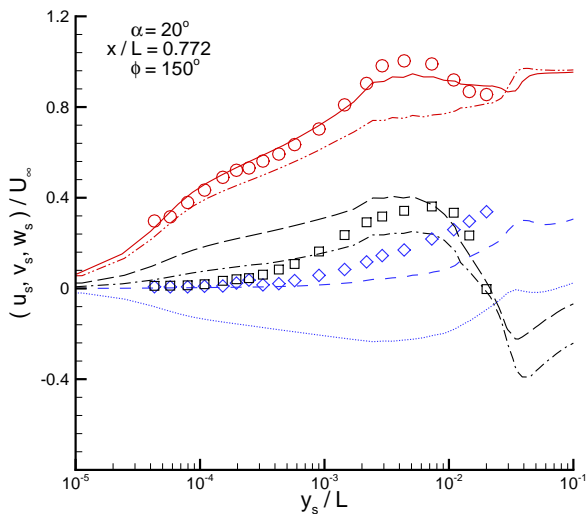


**Fig. 8** Mean velocity profiles for the static and maneuvering geometries at  $20^\circ$  angle of attack, streamwise location  $x/L = 0.772$ , azimuthal angle of  $\phi = 150^\circ$ . Legend same as Figure 6.

The  $v_s$  velocity component is normal to the surface, the  $w_s$  velocity is tangent to the spheroid and completes the right-handed coordinate system. The profiles shown below have been made dimensionless using the major-axis length  $L$  of the spheroid and freestream velocity  $U_\infty$ . Three sets of profiles are shown in the figures: static- $\alpha$  measurements from Chesnakas and Simpson [7], DES predictions of the static- $\alpha$  flow, and profiles from the pitchup case (plotted in the pitching reference frame). The profiles are shown for angle of attack  $\alpha = 20^\circ$  and at axial location  $x/L = 0.772$ . Profiles at four azimuthal angles, from  $\phi = 90^\circ$  to

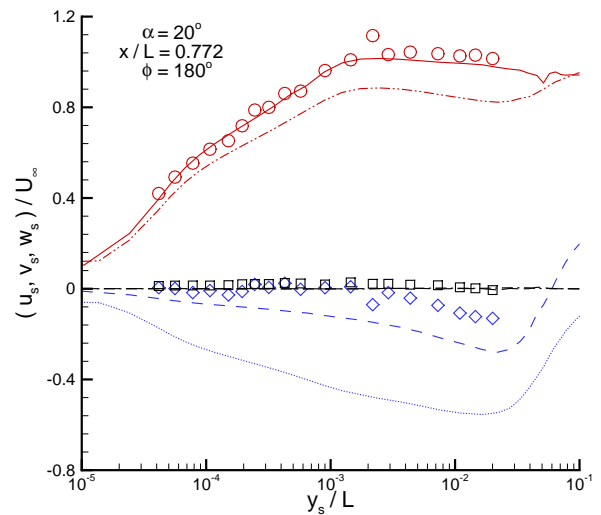


**Fig. 9** Mean velocity profiles for the static and maneuvering geometries at  $20^\circ$  angle of attack, streamwise location  $x/L = 0.772$ , azimuthal angle of  $\phi = 180^\circ$ . Legend same as Figure 6.

$\phi = 180^\circ$  ( $\phi = 0$  corresponds to the windward symmetry plane)

In Figure 6 the velocity profiles for the static geometry agree well with the measurements of Chesnakas and Simpson [7], the DES prediction accurately capturing the turning of the boundary layer at this location. Note that for the body-surface coordinate system the  $w_s$  profiles are negative, corresponding to the motion in the  $x = cst$  plane at  $\phi = 90^\circ$  being from the windward to the leeward side of the spheroid. The peak in  $w_s/U_\infty$  and its location at  $y_s/L = 3 \times 10^{-3}$  are accurately predicted. The  $u_s$  predictions are slightly larger than measured, though the agreement is adequate, both the predicted and measured profiles showing a logarithmic region. For the flow undergoing the pitchup maneuver the wall-normal gradient in  $u_s$  is slightly sharper and larger than the corresponding prediction and measurement of the static geometry  $u_s$  profile.

Shown in Figure 7 are the velocity profiles for the same conditions –  $\alpha = 20^\circ$ ,  $x/L = 0.772$  – at an azimuthal position further leeward at  $\phi = 120^\circ$ . Predictions of all three of the static-geometry velocity components agree very well with the measurements of Chesnakas and Simpson [7]. This azimuthal position is slightly leeward of the location of boundary layer detachment, the relatively sharp increase in the  $u_s$  and  $w_s$  profiles correspond to the trough of low-momentum fluid that accumulates between the primary vortex and body surface. The accurate prediction of the profiles at this location provide evidence that the prediction of boundary layer separation is relatively accurate. The  $w_s$  profile close to the wall is slightly positive, indicative of the influence of the primary vortex turning the

flow such that the  $w_s$  component, which lies in the  $x = \text{const}$  plane is beginning to sweep the near-wall fluid from windward side to leeward side.

At  $\phi = 150^\circ$ , for which the velocity profiles are shown in Figure 8, the streamwise velocity  $u_s$  prediction for the static geometry again agrees well with the measurements of Chesnakas and Simpson [7]. Compared to the profiles in Figure 7, the circumferential component  $w_s$  is more significant, reflective of the effect of the vortical structures developing from the primary separation (c.f., Figures 5). The figure shows that the  $w_s$  prediction for the static geometry is below the measurement in the region where the profile acquires its maximum and that the wall-normal velocities are also below the measured values. For the pitchup, the streamwise component shown is lower than in the static-geometry case.

Figure 9 shows the velocity profiles at  $\phi = 180^\circ$ , the leeward symmetry plane. As observed at the other azimuthal positions, the DES prediction of the  $u_s$  component for the static geometry agrees well with the measurements of Chesnakas and Simpson [7], the wall-normal velocity in the DES result being slightly larger than the measured values. For the pitchup, the streamwise velocity is lower than the static-geometry predictions and measurements. The wall-normal velocity in the pitchup is substantially larger than in the static-geometry DES and measurements, the profile indicating a flow towards the wall in the spheroid reference frame.

#### Skin-friction, pressure, forces and moments

Azimuthal distributions of the magnitude of the skin friction coefficient are shown in Figure 10 for  $\alpha = 20^\circ$  and Figure 11 for  $\alpha = 30^\circ$ . For both angles of attack, the distributions in the aft region are shown, for  $x/L = 0.729$  and  $x/L = 0.882$ . DES predictions are contrasted against the URANS results from Rhee and Hino [13] and the experimental measurements of Wetzel and Simpson [1]. For  $\alpha = 20^\circ$  (Figure 10), the DES predictions and URANS results of Rhee and Hino [13] yield similar distributions, the minima in the vicinity of  $\phi = 125^\circ$  correlating with the primary separation [23]. In general, for both axial stations at  $\alpha = 20^\circ$  the experimental measurements are above the two sets of simulation results. Unfortunately, the experimental values near the attachment line at  $\phi = 0$  are extraordinarily high and cannot be justified by a turbulent boundary layer (since such boundary layers never sustain skin-friction coefficients based on edge velocity over  $6 \times 10^{-3}$ , and the edge velocity is close to the freestream velocity), nor by a laminar boundary layer at the present Reynolds numbers. The qualitative behavior near the attachment line is also in strong contrast to CFD, precisely on the windward side where CFD is most reliable. If we imagine that CFD missed a relaminarization of the attachment-line

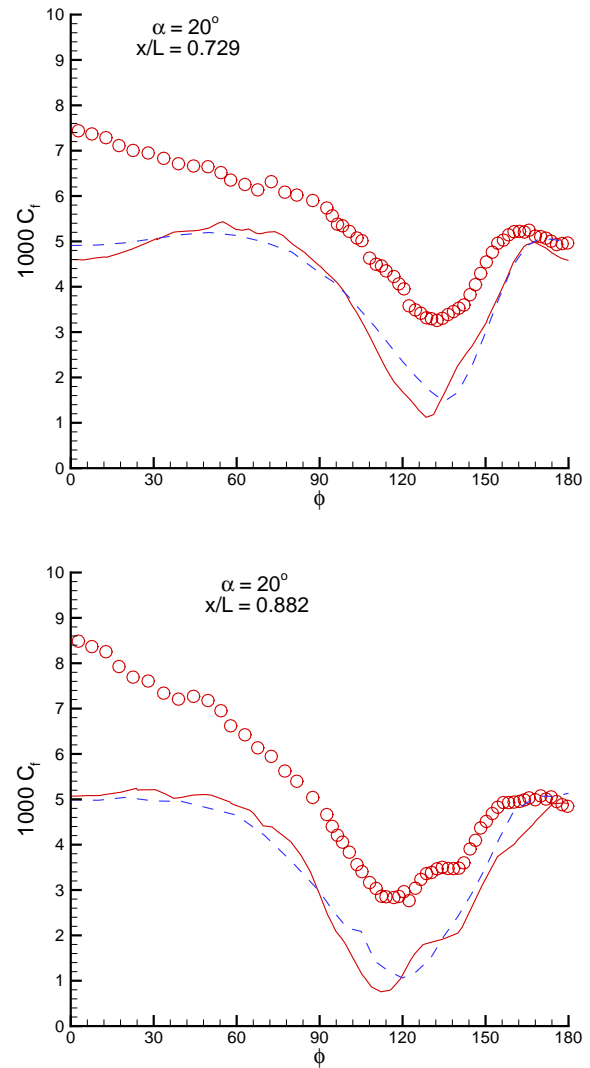


**Fig. 10** Azimuthal distribution of skin friction coefficient from the pitchup maneuver,  $\alpha = 20^\circ$ , streamwise locations  $x/L = 0.729, 0.882$ . — DES; ---- Rhee and Hino [13];  $\circ$  Wetzel and Simpson [1].

flow, this would result in the CFD skin friction being too high in that region, rather than too low. An independent measurement, for instance with a hot film or oil technique, would assist in clarifying issues related to the measurements.

At  $x/L = 0.882$ , minima in the DES predictions for  $\alpha = 20^\circ$ , correlate with boundary layer separation. As indicated by Figure 2, secondary separation is difficult to distinguish for the pitchup case, in turn consistent with the effectively lower angle of attack induced by the maneuver. For  $\alpha = 30^\circ$ , somewhat analogous features are observed, with the experimental measurements consistently above the simulation results. Compared to the distributions for  $\alpha = 20^\circ$ , the  $C_f$  minimum, correlated with the primary separation, occurs at lower azimuthal angles, corresponding

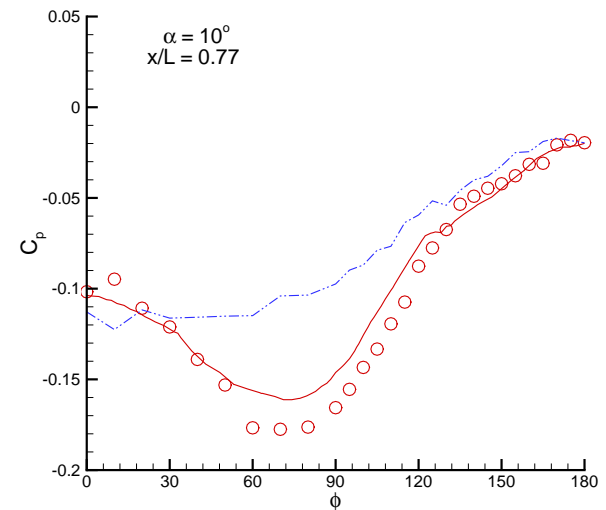
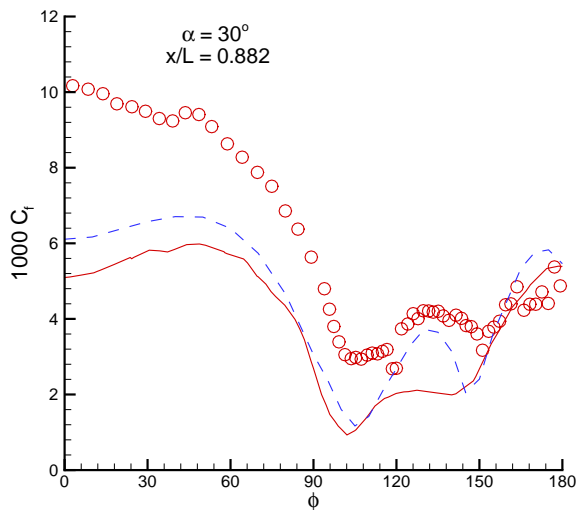
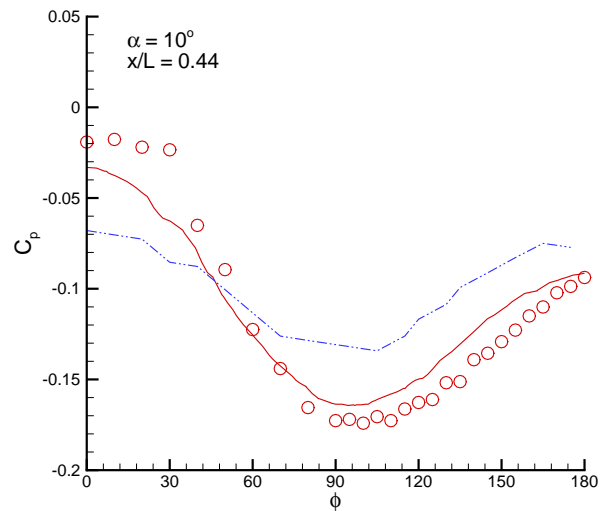
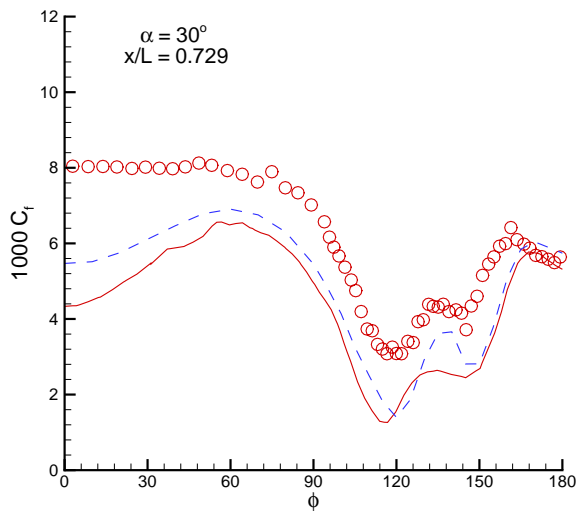


**Fig. 11** Azimuthal distribution of skin friction coefficient from the pitchup maneuver,  $\alpha = 30^\circ$ , streamwise locations  $x/L = 0.729, 0.882$ . — DES; ---- Rhee and Hino [13];  $\circ$  Wetzal and Simpson [1].

**Fig. 12** Azimuthal distribution of pressure coefficient from the maneuvering flow,  $\alpha = 10^\circ$ , streamwise locations  $x/L = 0.440, 0.770$ . — DES; ---- Rhee and Hino [13];  $\circ$  Hoang *et al.* [2].

to the location of the primary separation occurring at a more windward location with increasing  $\alpha$ . At the higher angle of attack, the second minima in  $C_f$  are more clearly defined.

Azimuthal variations in the pressure coefficient are shown in Figures 12-14 for  $\alpha = 10-30^\circ$ . For each angle of attack,  $C_p$  distributions are shown at axial locations  $x/L = 0.44$  and  $x/L = 0.77$ . DES predictions are plotted, along with the URANS results of Rhee and Hino [13] and experimental measurements of Hoang *et al.* [2]. For  $\alpha = 10^\circ$ , the agreement between the DES predictions and experimental measurements is reasonable, with the DES accurately capturing the peak-to-peak variation. The URANS prediction of Rhee and Hino [13] is also shown in Figure 12 and the figure shows less satisfactory agreement with the measured distribution

or DES result. At  $\alpha = 20^\circ$  in Figure 13 there is good agreement between the DES prediction at  $x/L = 0.44$  and experimental measurement. The URANS result from Rhee and Hino [13] shows fair agreement with the measured distribution. At  $x/L = 0.77$  in Figure 13, the second minima in  $C_p$  near  $\phi = 165^\circ$  is not predicted as accurately in the DES, though as also observed at  $x/L = 0.44$ , the DES prediction is closer to the measured distribution than the URANS. At  $\alpha = 30^\circ$  and  $x/L = 0.44$ , the  $C_p$  distribution in Figure 14 shows in the measured distribution from Hoang *et al.* [2] a second minima around  $\phi = 165^\circ$  that is not accurately predicted in the present DES or the URANS. At  $x/L = 0.77$ , the measured  $C_p$  for  $\phi > 110^\circ$  is relatively flat, characteristic of flow detachment from the spheroid. Both the present DES and URANS of Rhee and Hino [13] produce similar

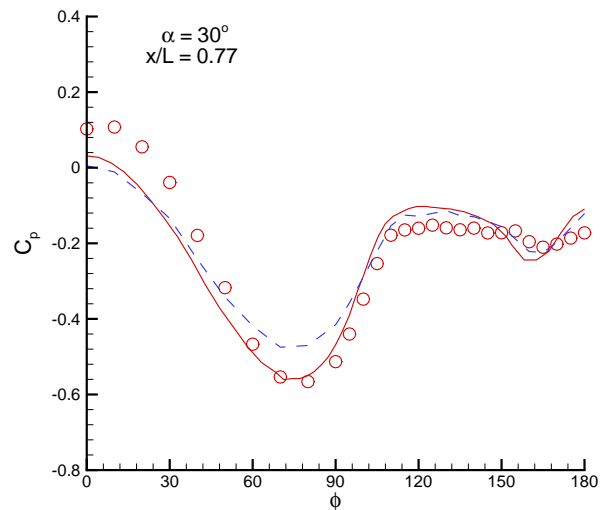
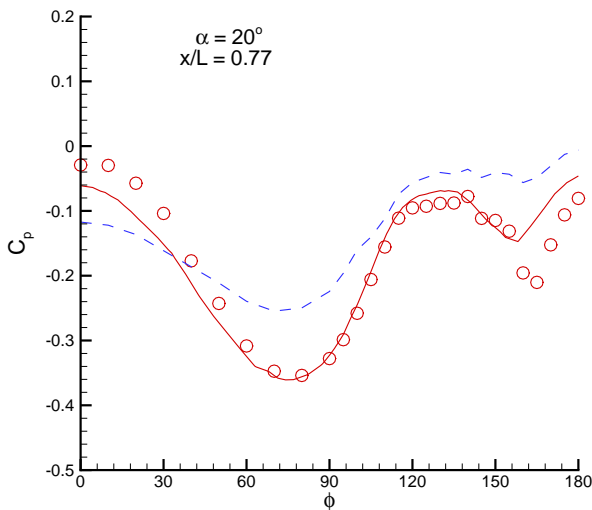
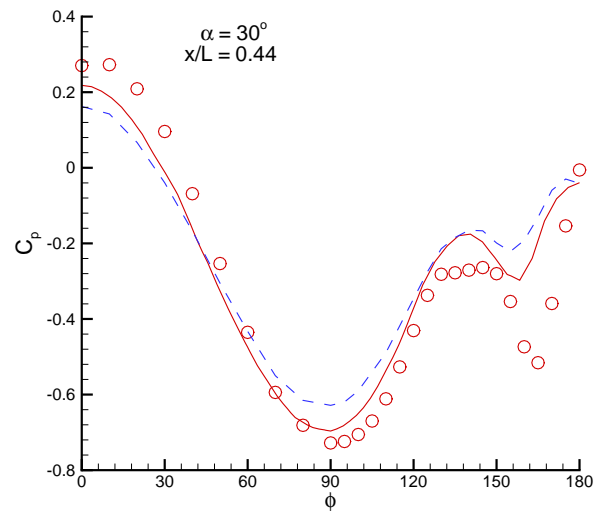
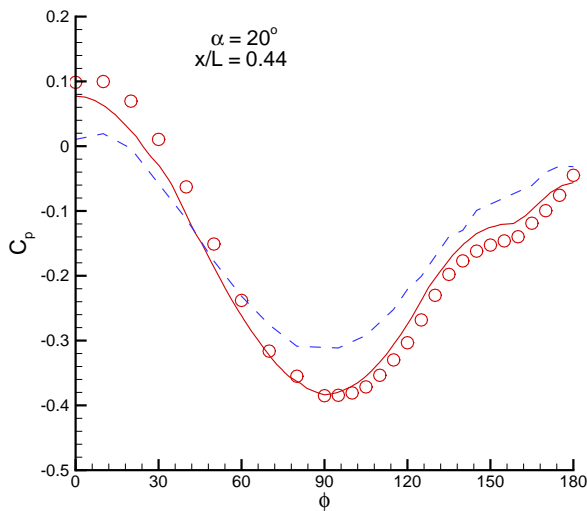


**Fig. 13** Azimuthal distribution of pressure coefficient from the maneuvering flow at  $\alpha = 20^\circ$ , streamwise locations  $x/L = 0.440, 0.770$ . — DES; - - - Rhee and Hino [13];  $\circ$  Hoang *et al.* [2].

**Fig. 14** Azimuthal distribution of pressure coefficient from the maneuvering flow at  $\alpha = 30^\circ$ , streamwise locations  $x/L = 0.440, 0.770$ . — DES; - - - Rhee and Hino [13];  $\circ$  Hoang *et al.* [2].

distributions as shown in the figure.

Figure 15 and Figure 16 shows the variation of the normal force coefficient  $C_z$  and pitching moment coefficient  $C_m$  with angle of attack, respectively. In general, the numerical results capture reasonably well the evolution with  $\alpha$  in  $C_z$  and  $C_m$ . The URANS predictions of Rhee and Hino [13] are adequate, though the normal force prediction is below the data.

### Summary

Flowfield predictions around a 6 : 1 prolate spheroid undergoing a pitchup maneuver were obtained using Detached-Eddy Simulation. Similar to the measurements of Wetzel and Simpson [1], the pitchup results in a lag in the development of the flow structure with the primary separation occurring further leeward, though the leeward shift in the primary separation was smaller

than measured. Comparison of the mean velocities in a body-surface coordinate system with experimental measurements of the static- $\alpha$  solutions shows that the development of the mean flow is accurately predicted.

Predictions of the azimuthal distribution of the skin friction exhibited similar variation as the measured values, though with a somewhat consistent shift below measurements. Measured  $C_f$  values are high, especially on the windward side. DES predictions of the skin friction distribution are similar to the URANS results of Rhee and Hino [13]. Development of the pressure field was accurately predicted, in better agreement with measurements than in Rhee and Hino [13]. The finer mesh resolutions compared to those used by Rhee and Hino [13] provide part of the explanation for the improved agreement with measurements. Additionally, the application of DES enables a more

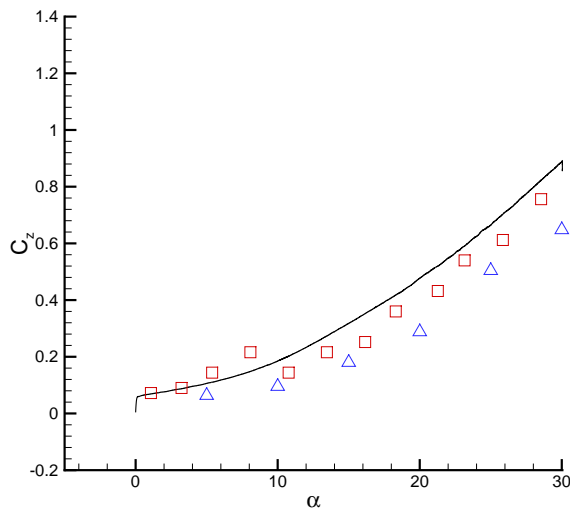


**Fig. 15 Normal force development against angle of attack. — DES;  $\square$  Wetzels and Simpsons [1];  $\triangle$  Rhee and Hino [13].**

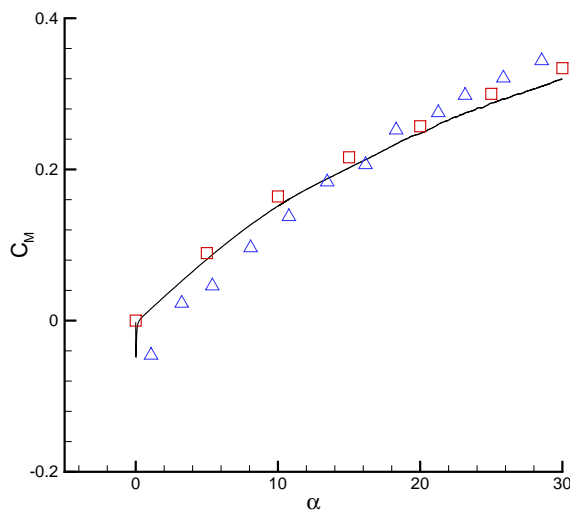


**Fig. 16 Pitching moment development against angle of attack. — DES;  $\square$  Wetzels and Simpsons [1];  $\triangle$  Rhee and Hino [13].**

coherent structure to be resolved in the wake, in the present case this effect is related to the reduction of the eddy viscosity in the lee side. The effect of mesh refinement remains to be ascertained in order to further assess the role of the model as well as other aspects of the computations.

#### Acknowledgments

The authors gratefully acknowledge the support of the Office of Naval Research (Grant N00014-99-1-0922, Program Officers: Dr. L. Patrick Purtell and Dr. Ron Joslin). The insight and helpful suggestions of Dr. Philippe R. Spalart have benefited the work throughout. The computations were performed at the

Maui High Performance Computing Center.

#### References

- <sup>1</sup> Wetzels, T.G. and Simpson, R.L., 1998, "Unsteady Crossflow Separation Location Measurements on a Maneuvering 6:1 Prolate Spheroid", *AIAA J.*, pp. 2063-2071.
- <sup>2</sup> Hoang, N.T., Wetzels, T.G. and Simpson, R.L., 1994, "Unsteady Measurements over a 6:1 Prolate Spheroid undergoing a Pitchup Maneuver", *AIAA Paper 94-0197*.
- <sup>3</sup> Forsythe, J.R. and Woodson, S.H., 2003, "Unsteady CFD Calculations of Abrupt Wing Stall using Detached-Eddy Simulation", *AIAA Paper 2003-0594*.
- <sup>4</sup> Barber, K. M., and Simpson, R. L., 1991, "Mean Velocity and Turbulence Measurements of Flow Around a 6:1 Prolate Spheroid", *AIAA Paper 91-0255*.
- <sup>5</sup> Ahn, S., 1992, "An Experimental Study of Flow over a 6 to 1 Prolate Spheroid at Incidence", Ph.D. Dissertation, Aerospace Engineering Dept., Virginia Polytechnic Inst. and State Univ., Blacksburg, VA.
- <sup>6</sup> Chesnakas, C. J., and Simpson, R. L., 1996, "Measurements of the Turbulence Structure in the Vicinity of a 3-D separation," *J. Fluids Eng.*, **118**(2), pp. 268-275.
- <sup>7</sup> Chesnakas, C.J. and Simpson, R.L., 1997, "Detailed investigation of the three-dimensional separation about a 6:1 prolate spheroid", *AIAA J.*, **35**(6), pp. 990-999.
- <sup>8</sup> Goody, M., Simpson, R. L., Engel, M., Chesnakas, C. J. and Devenport, W. J., 1998, "Mean Velocity and Pressure and Velocity Spectral Measurements Within a Separated Flow Around a Prolate Spheroid at Incidence," *AIAA Paper 98-0630*.
- <sup>9</sup> Tsai, C.-Y. and Whitney, A.K., 1999, "Numerical Study of Three-Dimensional Flow Separation for a 6:1 Ellipsoid", *AIAA Paper 99-0172*.
- <sup>10</sup> Rhee, S.H. and Hino, T., 2000, "Computational Investigation of 3D Turbulent Flow Separation around a Spheroid using an Unstructured Grid Method", *J. Soc. Naval Architects of Japan*, **188**, pp. 1-9.
- <sup>11</sup> Hedin, P.-O., Berglund, M., Alin, N. and Fureby, C., 2001, "Large eddy simulation of the flow around an inclined prolate spheroid", *AIAA Paper 2001-1035*.

- <sup>12</sup> Constantinescu, G.S., Pasinato, H., Wang, Y.-Q., Forsythe, J.R. and Squires, K.D., “Numerical investigation of the flow past a prolate spheroid”, 2002, *J. Fluids Eng.*, **124**(4), pp. 904-910.
- <sup>13</sup> Rhee, S.H. and Hino, T., 2002, “Numerical simulation of unsteady turbulent flow around a maneuvering prolate spheroid”, *AIAA J.*, **40**(10), pp. 2017-2026.
- <sup>14</sup> Spalart, P.R., 2000, “Strategies for Turbulence Modeling and Simulations”, *Int. J. Heat and Fluid Flow*, **21**, p. 252-263.
- <sup>15</sup> Spalart, P.R. and Allmaras, S.R., 1994, “A One-Equation Turbulence Model for Aerodynamic Flows,” *La Recherche Aerospatiale* **1**, pp. 5-21.
- <sup>16</sup> Spalart, P.R., Jou, W.H., Strelets, M. and Allmaras, S.R., 1997, “Comments on the Feasibility of LES for Wings, and on a Hybrid RANS/LES Approach,”, *First AFOSR International Conference on DNS/LES*, Ruston, Louisiana, USA.
- <sup>17</sup> Strelets, M., 2001, “Detached Eddy Simulation of Massively Separated Flows”, *AIAA Paper 01-0879*.
- <sup>18</sup> Shur, M., Spalart, P. R., Strelets, M., and Travin, A, 1999, “Detached-Eddy Simulation of an Airfoil at High Angle of Attack”, Proc. 4th Int. Symp. Eng. Turb. Modelling and Measurements.
- <sup>19</sup> Strang, W. Z., Tomaro, R. F, Grismer, M. J., 1999, “The Defining Methods of Cobalt<sub>60</sub>: a Parallel, Implicit, Unstructured Euler/Navier-Stokes Flow Solver,” *AIAA Paper 99-0786*.
- <sup>20</sup> Gottlieb, J.J. and Groth, C.P.T., 1988, “Assessment of Riemann Solvers for Unsteady One-Dimensional Inviscid Flows of Perfect Gases”, *J. Comp. Phys.*, **78**, pp. 437-458.
- <sup>21</sup> Karypis, G., Schloegel, K. and Kumar, V., 1997, “ParMETIS: Parallel Graph Partitioning and Sparse Matrix Ordering Library Version 1.0”, University of Minnesota, Department of Computer Science, Minneapolis, MN 55455.
- <sup>22</sup> Pirzadeh, S., 1996, “Three-dimensional Unstructured Viscous Grids by the Advancing Layers Method”, *AIAA J.*, **34**, pp. 43-49.
- <sup>23</sup> Wetzal, T.G., Simpson, R.L. and Chesnakas, C.J., 1998, “Measurement of three-dimensional crossflow separation”, *AIAA J.*, **36**(4), pp. 557-564.